Generation and control of ultrashort-wavelength two-dimensional surface acoustic waves at nanoscale interfaces

Qing Li, Kathleen Hoogeboom-Pot, Damiano Nardi, Margaret M. Murnane, and Henry C. Kapteyn
Department of Physics and JILA, University of Colorado and NIST, Boulder, Colorado, USA

Mark E. Siemens
Department of Physics and Astronomy, University of Denver, Denver, Colorado, USA

Erik H. Anderson
Center for X-Ray Optics, Lawrence Berkeley National Laboratory, Berkeley, California, USA

Olav Hellwig, Elizabeth Dobisz, and Bruce Gurney
San Jose Research Center, HGST, a Western Digital company, San Jose, California, USA

Ronggui Yang
Department of Mechanical Engineering, University of Colorado, Boulder, Colorado, USA

Keith A. Nelson
Department of Chemistry, Massachusetts Institute of Technology, Cambridge, Massachusetts, USA
(Received 2 February 2012; published 15 May 2012)

In this work, we generate and probe the shortest wavelength surface acoustic waves to date, at 45 nm, by diffracting coherent extreme ultraviolet beams from a suboptical phononic crystal. The short acoustic wavelengths correspond to penetration depths of approximately 10 nm. We also measure the acoustic dispersion in two-dimensional nanostructured phononic crystals down to this wavelength for the first time, showing that it is strongly influenced by the ultrashort acoustic penetration depth, and that advanced finite-element analysis is required to model the dispersion. Finally, we use pulse sequences to control surface acoustic wave generation in one-dimensional nanostructured gratings, to preferentially enhance higher-order surface waves, while suppressing lower frequency waves. This allows us to reduce the generated surface acoustic wavelength by a factor of two for a defined nanostructure period.

DOI: 10.1103/PhysRevB.85.195431 PACS number(s): 68.35.Iv, 78.20.Pa, 62.25.Fg, 43.35.Pt

I. INTRODUCTION

Surface acoustic waves (SAWs) are acoustic modes that propagate while confined within a very shallow penetration depth, enabling a broad range of applications in nondestructive material characterization and signal processing. With a penetration depth corresponding to a fraction of the acoustic wavelength,[1] nanometer-scale wavelength SAWs are needed to precisely characterize the mechanical properties of nanostructured materials and systems such as multilayers and thin films used in nanoelectronics and nano-bit-patterned data storage devices.

Various approaches have been used to generate short-wavelength SAWs. A traditional mechanical transducer generates SAWs with a frequency limited by the electronic response time.[2,3] Ultrafast laser pulses can be used to impulsively heat a sample, inducing lattice expansion so that SAWs are launched. By focusing a laser beam onto a small spot, broadband SAWs can be excited.[4] Alternatively, the interference between two overlapping laser beams can create a transient excitation grating and launch narrow-band SAWs.[5,6] However, the SAW wavelength excited by these techniques is limited by the wavelength of the pump laser beam, i.e., barely submicrometer scale for visible light. To overcome this limitation, metallic nanopatterned gratings can be optically excited to create shorter wavelength SAWs.[7–12] The wavelength of the SAW excited with nanopatterned structures is then only limited by the spatial period of the nanopattern.

Several approaches for detecting short-wavelength SAWs have been demonstrated, including monitoring the strain-induced transient reflectivity change[7–9] and using interferometric techniques to observe the refractive-index or optical phase changes induced by the surface displacement.[13] However, the resultant signals can be complicated to interpret. Recently, we used coherent extreme ultraviolet (EUV) beams, with wavelengths shorter than the SAW wavelength, to directly probe the SAW-induced surface displacement.[10] This results in an extremely sensitive probe because the induced phase change on the EUV beam is large. By exciting a prepatterned one-dimensional (1D) nickel nanograting-on-sapphire sample with a femtosecond infrared (IR) laser pulse, and detecting the resultant acoustic waves using an EUV beam, SAWs with wavelengths as short as 125 nm were measured for the first time.[10] In addition to SAWs, quasiballistic thermal transport can be detected because of the high sensitivity of the coherent EUV probe to surface displacements at the picometer level and below.[10,14,15] However, to date, it was not clear if acoustic signals from $\ll$100-nm-scale nanostructures, with their significantly lower scattering efficiency, would be detectable, especially in two-dimensional (2D) phononic crystals where the scattered light is less than in the case of a one-dimensional grating.

In this work, we show that we can generate and probe the shortest wavelength surface acoustic waves to date, at 45 nm, with corresponding penetration depths of about 10 nm. This result is significant for nanoscale materials physics because it makes it possible to selectively probe the mechanical properties of very thin films and interfaces as well as nanostructures deposited on, or embedded within, a surface for the first time. We also characterize the acoustic dispersion of these nanostructures that is strongly influenced by the varying penetration depth into the sample. Moreover, to understand and model acoustic dispersion in these 2D phononic crystals, finite element simulations are required, because simple approximations can no longer be used (as in the case for 1D phononic crystals). Finally, we use laser pulse sequences to control SAW generation in 1D nanostructures, and preferentially enhance higher-order SAWs, while suppressing lower frequency waves. This allows us to reduce the generated SAW wavelength and, consequently, the SAW penetration depth by a factor of two with respect to the spatial period set by the suboptical phononic crystal. This has important implications for the ultimate physical limits that one can probe using acoustic metrology.

II. GENERATING SURFACE ACOUSTIC WAVES IN 2D NANOSTRUCTURED SAMPLES

For this experiment, we split the output of a Ti:Sapphire amplifier (2 kHz, 2 mJ, 800 nm, 30 fs) into pump and probe beams, as shown in Fig. 1. The pump beam is loosely focused onto the sample to impulsively heat the nanostructured grating and launch SAWs. In order to uniformly heat the nanostructures, the pump beam spot is relatively large, around 600 μm in diameter, with a fluence of 8 mJ/cm^2. The probe beam is focused into a gas-filled hollow waveguide, to generate extreme ultraviolet beams using the high harmonic generation (HHG) process, that span a range of wavelengths centered at 30 nm. The pulse duration of the harmonics are even shorter than the femtosecond laser pulse, and the output HHG beams are fully spatially coherent when the frequency upconversion process is fully phase matched.[16] The HHG probe beam passes through two thin Al filters, which block IR laser light and low-order harmonics, before being refocused by a toroidal mirror to a diameter of $\approx$100 μm on the sample. The diffracted HHG signal is then monitored by an x-ray sensitive CCD camera.

The samples consist of 1D and 2D nanograting samples, as shown in Fig. 1. Three different nanogratings were prepared using electron beam lithography and lift-off techniques, covering multiple 150 μm $\times$ 150 μm regions. The first sample (sample I) was similar to that used in our previous experiment,[10] consisting of a 20-nm high 1D nickel nanograting on an isotropic sapphire substrate, and it was used as a data check. The width L of the nickel stripes varied between 65 nm and 1 μm, with a fixed duty cycle of 25%, so that the grating period $P = 4L$. The second sample consisted of 2D arrays of 15-nm-high nickel pillars on an isotropic sapphire substrate, with nominal pillar widths L ranging from 40 nm to 1 μm, also at a fixed 25% duty cycle. These two samples can be usefully compared with each other to study the effect of dimensionality. Finally, our sample III had geometry similar to sample II, but with perpendicularly anisotropic Co/Pd multilayer pillars, which are of great interest because they are commonly used as a model system for bit patterned media (BPM).[17,18] This Co/Pd grating consisted of 15-nm-high multilayer pillars of width L ranging from 30 nm to 1 μm patterned on a crystalline silicon substrate along the Si(100) direction, with grating periodicities ranging from 45 nm to 1.2 μm.[19]

Sapphire is transparent to the 800-nm pump light, and silicon has a relatively long absorption depth at this wavelength. Therefore the pump laser pulse is absorbed mainly by the nanostructures, heating them rapidly. The laser energy is first absorbed by electrons; subsequently, fast electron-electron and electron-phonon scattering rates rapidly establish thermal equilibrium within the metallic nanostructures on subpicosecond time scales.[20] Sudden expansion of the metal lattice induces stress at the nanostructure/substrate interface and launches acoustic vibrations in different directions: surface acoustic waves are localized along the interface of the nanostructure/substrate system, while longitudinal acoustic waves propagate into the substrate. The resulting displacement is monitored by measuring the changes in the diffraction efficiency of the EUV probe beam as a function of pump-probe delay. The relative change in EUV diffraction signal in this experiment is about 3%, which is at least 10 times higher than that observed using optical probe techniques.[7–9,11] As

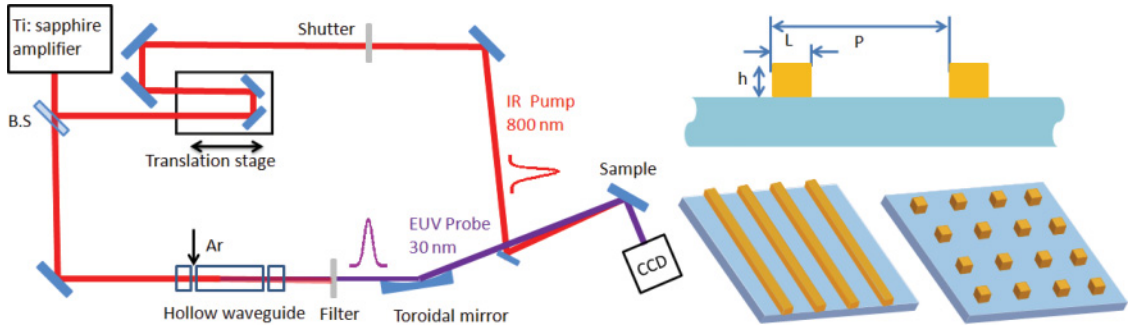

FIG. 1. (Color online) (Left) Schematic diagram of the experimental setup: a femtosecond IR pump beam is focused onto the nanostructured sample to generate SAWs. The HHG beam probes the time-dependent surface displacement as a function of time delay between the pump and probe beams. (Right) Nanograting sample: the height h, nanopattern lateral size L, and periodicity P are indicated for both 1D and 2D nanogratings.

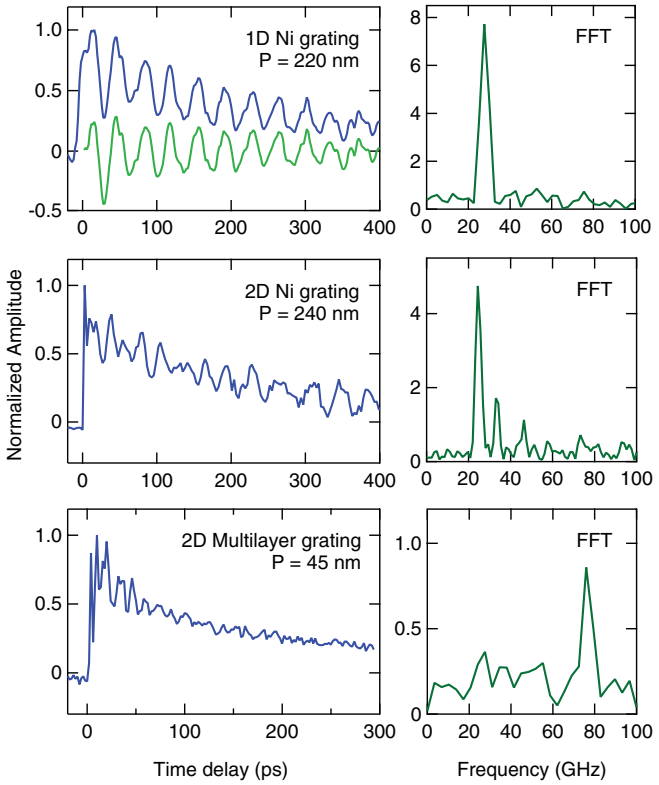

FIG. 2. (Color online) SAW oscillation signal as a function of pump-probe delay for three samples. The SAW signal is extracted by removing the slowly decaying thermal signal (which transforms the blue curve to the green curve in the top left graph). A Fourier transform is applied to obtain the frequency spectrum. The top graph shows the SAW signal and spectrum for 1D Ni-on-sapphire nanogratings with period 220 nm, the middle graph plots the same for 2D Ni-on-sapphire nanopillars with 240-nm period, while the lower graph plots SAWs from 2D Co/Pd multilayer pillars of period 45 nm on Si.

explained below, this makes it possible to observe, study, and control short wavelength SAW dynamics.

Figure 2 shows typical SAW signals from three samples: (from top to bottom) 1D Ni nanogratings of line width 65 nm and periodicity 220 nm, 2D Ni nanopillars of line width 60 nm and periodicity 240 nm, and 2D multilayered Co/Pd nanopillars of line width 30 nm and periodicity 45 nm. The fast rising and slowly decaying signal components are caused by pump beam-induced thermal expansion and subsequent heat dissipation from the nanostructure into the substrate.[15] The fast oscillation signal is due to the propagating surface acoustic waves. The thermal signal can be removed by using a simplified exponential fit, while a Fourier transform is performed to extract the SAW frequencies, as shown in Fig. 2.

By comparing the spectra of 1D and 2D nanostructured samples in the top and middle graphs of Fig. 2, it is very clear that more SAW frequencies are generated for the 2D sample compared with the 1D case. In the frequency spectrum of the 2D sample, the lowest acoustic frequency corresponds to the fundamental SAW frequency f_0, while the second peak is associated with SAWs with a frequency $\sqrt{2}f_0$ corresponding to the diagonal periodicity. The third peak corresponds to the second order SAW frequency, which is approximately $2f_0$. Shorter wavelength (higher frequency) SAWs correspond to stronger surface confinement. The lower graph of Fig. 2 plots the SAW spectrum from 2D Co/Pd multilayer pillars on Si. Due to the small pillar width (30 nm) and periodicity (45 nm) in this sample, the fundamental SAW wavelength of 45 nm corresponds to the shortest wavelength SAW observed to date. The propagation of higher-order SAWs in the multilayer pillar sample appears to be weaker than in the nickel-on-sapphire sample. However, the damping rate will depend on many factors such as interface properties and SAW frequency.

Measuring how the SAW velocity changes with wavelength is important for characterizing nanostructures, interfaces, and thin films. For the complex 2D phononic crystals studied here, SAW frequencies as a function of wavenumber for samples II and III are plotted in Fig. 3. Each SAW wavenumber corresponds to a different nanograting period. In the case of the nickel-on-sapphire sample II, three SAW frequencies are shown, corresponding to the SAW wave vector orientation with

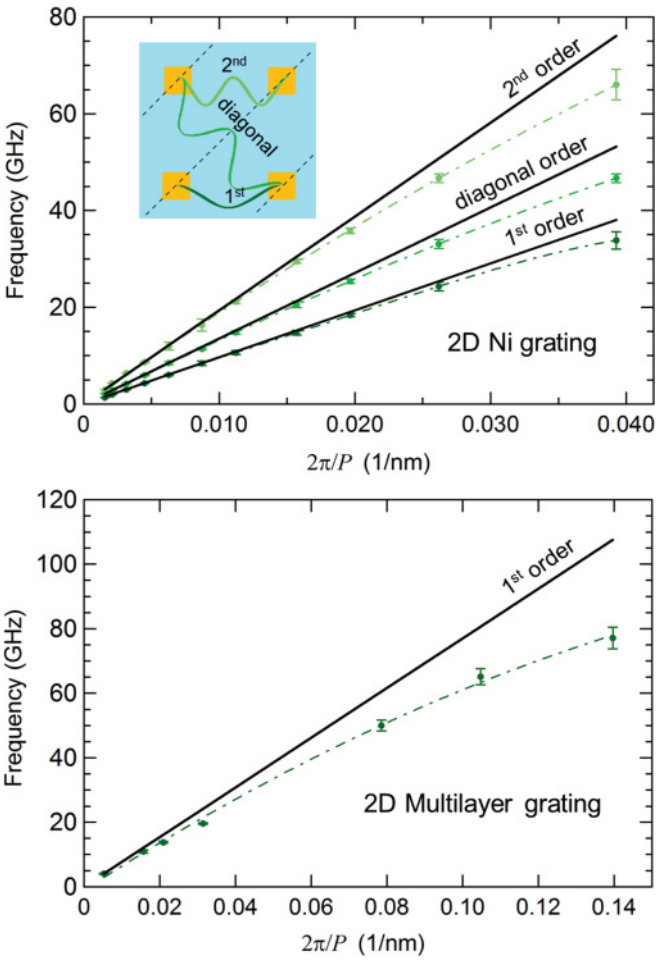

FIG. 3. (Color online) Dispersion relations: frequency as a function of fundamental-order wavenumber $k = 2\pi/P$. (Top) Fundamental, diagonal and second order SAW frequencies for the 2D nickel-on-sapphire sample II. The inset shows the various SAWs. (Bottom) Fundamental SAW on the Co/Pd multilayer-on-silicon sample III. The solid lines show the Rayleigh acoustic velocity of the substrate multiplied by the SAW order. The dashed line is intended as a guide to the eye.

respect to the nanograting, as pictured in the inset. To better distinguish these orders in the figure, all frequencies are plotted as a function of the fundamental wavenumber k_1 ($k_1 = 2\pi/P$). The phase velocity of the SAW is given by $v = \omega/k$, thus v can be extracted directly from the measurement. Compared with the fundamental k_1, higher order SAWs have shorter wavelengths and larger wavenumbers, by a factor of $\sqrt{2}$ for the diagonal order and by 2 for the second order. Their velocity can be calculated accordingly. The solid line represents a fit to the velocity corresponding to the first few data points, i.e., the lowest values of k or longest SAW wavelengths and penetration depths. The velocity extracted from the fundamental SAW is 6040 m/s—consistent with the Rayleigh acoustic velocity of the isotropic sapphire substrate. The velocities extracted from the diagonal and second-order SAWs are 5920 and 5980 m/s, respectively. In sample III (Co/Pd multilayer phononic nanocrystal sample), only the fundamental SAW dispersion relation is plotted, and the 4840 m/s velocity extracted from the fundamental SAW is in agreement with the Rayleigh acoustic velocity of the Si(100) substrate.

The higher wavenumber k (shorter wavelength) data plotted in Fig. 3 clearly deviate from the constant Rayleigh velocity, indicating that the speed of the SAWs decrease with wavelength (i.e., periodicity of the nanogratings). To further explore this trend, we plot the SAW velocity as a function of wave number for fundamental, diagonal, and second orders, as shown in Fig. 4 for sample II. It is clear that there is significant deviation from the Rayleigh velocity of sapphire (horizontal solid line). In order to explain this behavior, two approaches were explored. First, we considered an effective mass-loading approximation. Because the SAW velocity in the metal nanostructure is slower than that in the substrate for all of

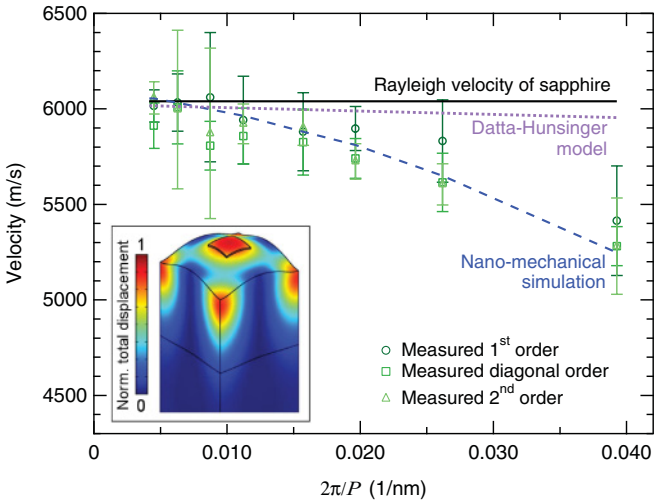

FIG. 4. (Color online) Velocity dispersion for the 2D nickel-on-sapphire sample II for the fundamental, diagonal and second-order SAW oscillations. The black solid line shows the Rayleigh velocity of the sapphire substrate. The velocities extracted from the fundamental, diagonal and second-order measurement are shown as circles, squares, and triangles, respectively. The purple dotted line is based on the Datta and Hunsinger approximation, while the blue dashed line is from a finite element simulation. In the inset we report the total displacement profile of the generated fundamental SAW, as calculated by finite element simulations.

the samples, the nanostructure will slow the SAW propagation. As the period of the nanostructures, and thus SAW wavelength, get smaller, the SAW penetration depth decreases so that it is more confined in the nanostructure, which contributes to the deviation from the Rayleigh velocity of the sapphire substrate. When reducing the period of the nanostructures at a fixed duty cycle, the height of the nanostructure does not scale down accordingly but remains constant. The mass of the nanostructure is thus not proportionally decreasing and the surface mass density is higher for the smaller gratings, resulting in a decreasing SAW speed. An effective mass-loading model, derived from thin film theory using the Datta and Hunsinger approximation,[21] is shown as a dotted purple line in Fig. 4. This approximation worked well in previous experiments using 1D nanostructures, which could reasonably be compared to thin films. However, the surface coverage is much lower in 2D nanostructured gratings, and as a result, the Datta and Hunsinger model under predicts the SAW dispersion by an order of magnitude.

A more accurate method to reproduce the dispersion of SAW velocity in 2D phononic crystals is based on first-principles modeling of the thermomechanics of impulsively excited samples using finite element simulations.[22,23] We calculate the spatially modulated heat-driven initial expansion of the nanograting. The resulting displacement field is projected over the set of eigenmodes of the nanostructured sample, which are solutions of the acoustic eigenvalue problem. This technique unambiguously resolves which eigenmodes are impulsively excited. The main contribution to the sample dynamics is thus revealed as a symmetric SAW, as reported in the inset of Fig. 4, and we can directly determine its frequency. This is the first time this technique has been applied for nanostructures less than 200 nm in lateral size in a 2D geometry. The fundamental SAW-velocity result of this finite element analysis is shown as a blue dashed line in Fig. 4, and it is in agreement with the data.

While we can explain the deviation from the Rayleigh velocity by considering the properties of both the nanostructure and substrate, we can also learn about those properties from the dispersion relation. By measuring the frequency changes as a function of SAW wavelength using this phononic crystal, information about the mechanical properties of the nanostructure and substrate can be extracted and related to each other. This offers a new method for surface metrology using picosecond SAWs at ultrashort wavelengths.

III. GENERATING AND SELECTIVELY ENHANCING HIGHER-FREQUENCY SAWS USING PULSE SEQUENCES

An attractive approach for generating shorter wavelength SAWs relies on modifying the pump pulse that generates the photoacoustic response so that higher-order SAWs (shorter wavelength) can be enhanced while suppressing lower orders. To control the SAW generation, we apply a two-pulse sequence to the sample, matched to the SAW we are trying to generate, as shown in Fig. 5. A similar strategy has been used to select and enhance bulk acoustic waves.[24–26] The pump beam is sent into a Michelson interferometer, which exploits a 50% beam splitter to generate two pump pulses with a relative delay that can

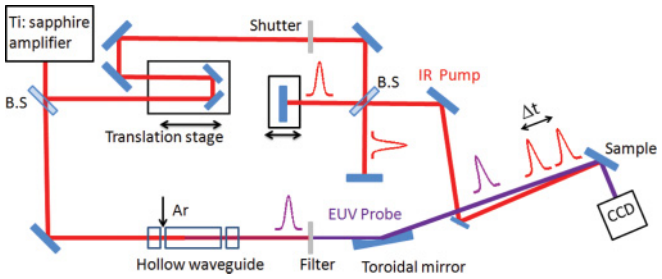

FIG. 5. (Color online) Schematic of the modified experimental setup: a Michelson interferometer is introduced to produce a two-pulse pump sequence.

be adjusted by simply moving a translation stage on one arm of the interferometer. To validate this technique, we used the simplest 1D nickel-on-sapphire sample I. In this configuration, the second pump pulse induces an additional stress on the Ni-sapphire interface, and a second surface acoustic wave is generated that will reinforce or reduce the first wave depending on their relative phase. Varying the time delay between the two pump pulses, we introduce a relative phase shift in the generated SAW sequence.

Typical time-resolved SAW signals are shown in the top three curves of Fig. 6, where the sample used was a 1D Ni-on-sapphire grating of line width $L = 220$ nm and periodicity $P = 800$ nm. The bottom curve in Fig. 6 represents the pure surface acoustic signal after removing the thermal relaxation dynamics.

Figure 7 shows the photoacoustic response from the same grating as in Fig. 6 (with the thermal background removed) at different relative delay times Δt between pump pulses.

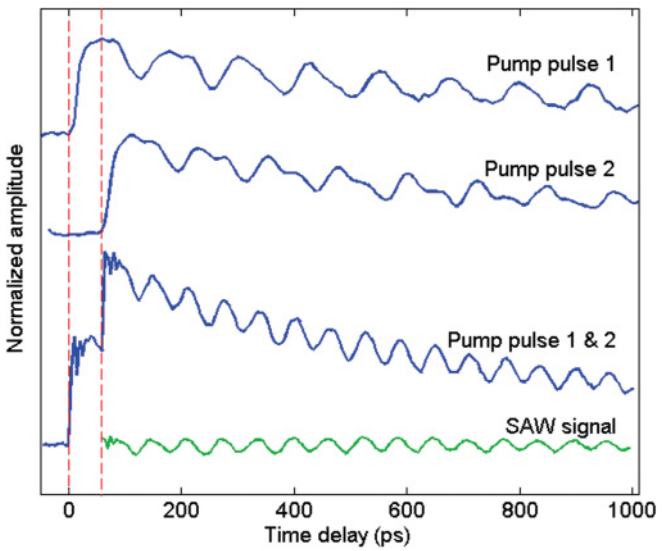

FIG. 6. (Color online) Time-resolved SAW signal from two-pulse pump sequence on a 1D Ni-on-sapphire sample with $P = 800$ nm (amplitudes of the top three curves are normalized and shifted for presentation). From top to bottom shows the signal with the pump pulse 1 only, pump pulse 2 only, and the two-pulse sequence SAW signal before (blue line) and after (green line) removing thermal relaxation dynamics. Pump pulse 1 is synchronized with the probe beam and pump pulse 2 arrives 62 ps later, as indicated by the vertical dashed lines.

The dynamic signal and the Fourier transform spectrum demonstrate the coherent interference from two SAWs, which can be directly controlled by adjusting the time delay between pulses.

Note that the delay Δt corresponds to a phase shift of $\Delta t/T_1$ for the fundamental SAW mode, where T_1 is its oscillation period. For the second order SAW mode with oscillation period T_2, the phase shift is $\Delta t/T_2$. From the photoacoustic frequency spectrum, the second order SAW period is about half of the fundamental value, i.e., $T_2 \approx T_1/2$. From the spectrum of Fig. 7, when both pump pulses arrive at the same time, we excite the SAW at the fundamental frequency 8.12 GHz (with a period of $T_1 = 123$ ps). The second-order frequency at 16.24 GHz is relatively weaker. For arbitrary relative time delay Δt between the two pump pulses, the total signal S can be described quantitatively as follows:

$$\begin{aligned} S = \theta(t)\Bigg[& A_1 \exp\left(-\frac{t}{\tau_1}\right)\cos(\omega_1 t + \Phi_1) \\ & + A_2 \exp\left(-\frac{t}{\tau_2}\right)\cos(\omega_2 t + \Phi_2)\Bigg] \\ & + \theta(t-\Delta t)\Bigg\{A_1 \exp\left(-\frac{t-\Delta t}{\tau_1}\right)\cos[\omega_1(t-\Delta t)+\Phi_1] \\ & + A_2 \exp\left(-\frac{t-\Delta t}{\tau_2}\right)\cos[\omega_2(t-\Delta t)+\Phi_2]\Bigg\}, \end{aligned} \tag{1}$$

where SAWs are described by a sinusoidal function, $\theta(t)$ is a unit step function, A_1 and A_2 are the SAW amplitudes for the fundamental and second order, τ_1 and τ_2 are the damping rates for both frequencies which depend only on the materials, Φ is the initial phase for SAWs, ω_1 and ω_2 are the frequencies for both waves. For the case considered here, where $\omega_2 = 2\omega_1 = 2\omega$, Eq. (1) can be rearranged after the second pump pulse arrives as

$$\begin{aligned} S_\omega = {} & A_1 \exp\left(-\frac{t}{\tau_1}\right)\Bigg\{\cos(\omega t + \Phi_1) \\ & + \exp\left(\frac{\Delta t}{\tau_1}\right)\cos\left[\omega(t-\Delta t)+\Phi_1\right]\Bigg\} \\ & + A_2 \exp\left(-\frac{t}{\tau_2}\right)\Bigg\{\cos(2\omega t + \Phi_2) \\ & + \exp\left(\frac{\Delta t}{\tau_2}\right)\cos[2\omega(t-\Delta t)+\Phi_2]\Bigg\}. \end{aligned} \tag{2}$$

For a relative delay between the two pump pulses of $\Delta t = T_1/2 = \pi/\omega$, a π-phase shift in the fundamental order is introduced by the second acoustic wave, resulting in destructive interference (see Fig. 7). Since $T_1/2 \sim T_2$, this delay time corresponds to a 2π-phase shift for the second-order SAW, resulting in constructive interference. From Eq. (2), it is clear that for this delay time the SAW signal can be simplified as

$$\begin{aligned} S_{T/2} = {} & A_1 \exp\left(-\frac{t}{\tau_1}\right)\left[1 - \exp\left(\frac{\pi}{\omega\tau_1}\right)\right]\cos(\omega t + \Phi_1) \\ & + A_2 \exp\left(-\frac{t}{\tau_2}\right)\left[1 + \exp\left(\frac{\pi}{\omega\tau_2}\right)\right]\cos(2\omega t + \Phi_2). \end{aligned} \tag{3}$$

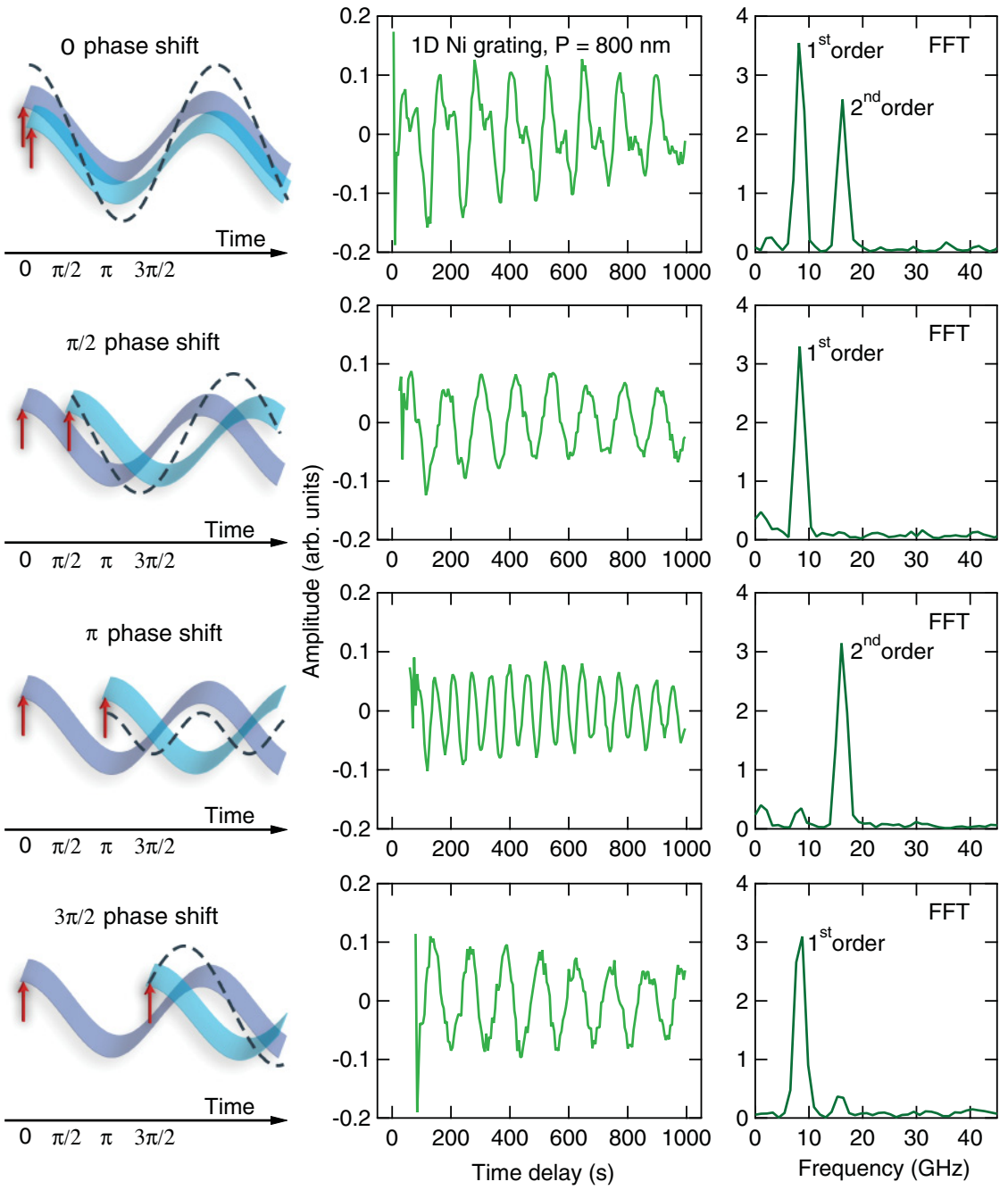

FIG. 7. (Color online) Fundamental and second-order SAWs in a 1D nanograting of 800-nm period, generated by two pump beams separated by varied time delays. Top to bottom: pumping scheme, extracted SAW signal and frequency spectrum for relative time delays of 0, 31, 62, and 93 ps, corresponding to phase shifts between the fundamental SAWs of 0, $\pi/2$, π, $3\pi/2$. Selective control of SAW generation is demonstrated.

The damping rates τ_1 and τ_2 are relatively long in sample I, and thus the exponential decay $\exp(\frac{\Delta t}{\tau_1}) = \exp(\frac{\pi}{\omega\tau_1})$ term is close to 1. The amplitude of the first term in Eq. (3), (the fundamental SAW), is close to zero, while the second term (the second-order SAW) is strongly reinforced. For the 800-nm-period grating, the required relative delay between the two pump pulses to enhance the second order is around 62 ps. Conversely, for time delays of 31 and 93 ps (corresponding to $\pi/2$ and $3\pi/2$ fundamental phase shifts), the fundamental frequency is enhanced while the second order SAWs interfere destructively.

The same approach also works for smaller 1D nanogratings (sample I). For the smallest sample—a 220-nm-period grating—the SAW signal as a function of pump-probe delay time, for phase shifts of 0 and π between the two pump pulses, are shown in Fig. 8. The top left curve in Fig. 8 matches the 1D sample plot in Fig. 3 very well, as expected since a single pulse excites SAWs in a 1D grating in both cases. Comparing the results from 0 and π phase shifts between the two pump pulses, the Fourier transforms clearly demonstrate that the fundamental order dominates in Fig. 8 top right with no visible second-order frequency in the

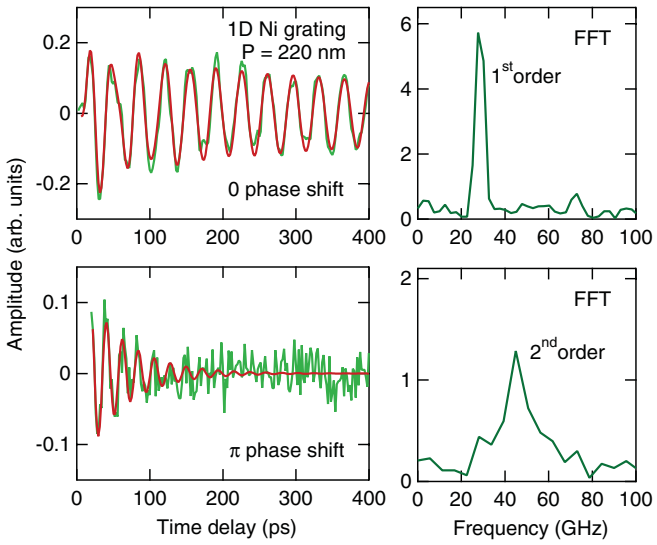

FIG. 8. (Color online) Controlling SAW generation in a $P = 220$ nm nanograting for zero (top left) and π (lower left) phase differences between the two pump pulses. The FFT on the lower right demonstrates selective enhancement of the second order with suppression of fundamental order SAWs.

spectrum, while the second order is enhanced in Fig. 8 lower right.

We fit our SAW data to Eq. (2) for each of these two cases to provide more information about the frequency and the damping of SAWs. At 0 phase shift, the curve fitting yields oscillation frequencies of $\omega_1 = 28.44 \pm 0.04$ GHz and $\omega_2 = 47.9 \pm 0.6$ GHz, with damping times of $\tau_1 = 756 \pm 141$ ps and $\tau_2 = 59 \pm 14$ ps. For the π-phase shift case, $\omega_2 = 45.6 \pm 0.5$ GHz and $\tau_2 = 58 \pm 11$ ps. The consistent values of ω_2 and τ_2 show that the same second-order SAW is preserved and reinforced while the fundamental order is suppressed.

Although a similar Michelson interferometer setup has been used in previous photoacoustic experiments that used visible light to pump and probe the SAWs,[27] due to the lower signal-to-noise ratio of the transient optical signal, it has not been possible to observe the selective enhancement of the second-order SAW until now. The sensitivity of the short-wavelength EUV probe allows us to observe this control for the first time, allowing the wavelength and penetration depth of the SAW to be reduced by a factor of two for a fixed nanopatterned phononic crystal. The same approach can be extended to 2D phononic crystals and higher SAW frequencies. In the future, two-pulse excitation could be extended to a pulse train designed to allow even more precise control over the generation and propagation of SAWs.

IV. CONCLUSIONS

In conclusion, we demonstrated two approaches for generating very short wavelength surface acoustic waves using EUV photoacoustic metrology. First, using 2D nanostructured gratings with periodicity as short as 45 nm, we generated and probed the shortest wavelength SAWs to date. These correspond to SAWs with penetration depths of only approximately 10 nm, leading to large deviations in the acoustic dispersion from that of the substrate that require numerical modeling to reproduce. The diagonal and second-order waves were also observed in the 2D sample geometry. Second, we used two-pulse sequences to selectively enhance either the fundamental or second order SAWs by controlling the relative delay between pump pulses. This allowed us to generate even shorter-wavelength SAWs in an existing nanopatterned phononic crystal sample. Combining these two techniques would result in generation and control of even shorter wavelength SAWs, and therefore access to even smaller penetration depths to enable highly sensitive characterization of ultrathin films and nanostructured interfaces.

ACKNOWLEDGMENTS

We thank Alex Maznev for valuable discussions. The JILA group acknowledges support from the US Department of Energy, Office of Basic Energy Sciences, and the NSF Engineering Research Center for Extreme Ultraviolet Science and Technology. R.Y. acknowledges his CAREER Award from NSF.

[1] B. Auld, *Acoustic Fields and Waves in Solids*, Vol. I (Wiley, New York, 1973).
[2] T. M. Reeder *et al.*, US Patent No. 3978731 (7th September 1976).
[3] H. Okano, N. Tanaka, Y. Takahashi, T. Tanaka, K. Shibata, and S. Nakano, Appl. Phys. Lett. **64**, 166 (1994).
[4] D. Schneider, Th. Witke, Th. Schwarz, B. Schoneich, and B. Schultrich, Surf. Coat. Technol. **126**, 136 (2000).
[5] J. A. Rogers, L. Dhar, and K. A. Nelson, Appl. Phys. Lett. **65**, 312 (1994).
[6] R. I. Tobey, M. E. Siemens, M. M. Murnane, H. C. Kapteyn, D. H. Torchinsky, and K. A. Nelson, Appl. Phys. Lett. **89**, 091108 (2006).
[7] B. Bonello, A. Ajinou, V. Richard, P. Djemia, and S. M. Cherif, J. Acoust. Soc. Am. **110**, 1943 (2001).
[8] D. H. Hurley and K. L. Telschow, Phys. Rev. B **66**, 153301 (2002).
[9] G. A. Antonelli, P. Zannitto, and H. J. Maris, Physica B - Condensed Matter **316**, 377 (2002).
[10] M. Siemens, Q. Li, M. Murnane, H. Kapteyn, R. Yang, E. Anderson, K. Nelson, Appl. Phys. Lett. **94**, 093103 (2009).
[11] C. Giannetti, B. Revaz, F. Banfi, M. Montagnese, G. Ferrini, F. Cilento, S. Maccalli, P. Vavassori, G. Oliviero, E. Bontempi, L. E. Depero, V. Metlushko, and F. Parmigiani, Phys. Rev. B **76**, 125413 (2007).
[12] J.-F. Robillard, A. Devos, and I. Roch-Jeune, Phys. Rev. B **76**, 092301 (2007).
[13] D. Hurley and O. Wright, Opt. Lett. **24**, 1305 (1999).
[14] R. I. Tobey, M. E. Siemens, O. Cohen, M. M. Murnane, H. C. Kapteyn, and K. A. Nelson, Opt. Lett. **32**, 286 (2007).

[15]M. E. Siemens, Q. Li, R. Yang, K. A. Nelson, E. H. Anderson, M. M. Murnane, and H. C. Kapteyn, Nat. Mater. **9**, 26 (2010).

[16]R. A. Bartels, A. Paul, H. Green, H. C. Kapteyn, M. M. Murnane, S. Backus, I. P. Christov, Y. Liu, D. Attwood, and C. Jacobsen, Science **297**, 376 (2002).

[17]O. Hellwig, T. Hauet, T. Thomson, E. Dobisz, J. D. Risner-Jamtgaard, D. Yaney, B. D. Terris, and E. E. Fullerton, Appl. Phys. Lett. **95**, 232505 (2009).

[18]M. Grobis, E. Dobisz, O. Hellwig, M. Schabes, T. Hauet, G. Zeltzer, and T. Albrecht, Appl. Phys. Lett. **96**, 052509 (2010).

[19]The exact sample structure used was Ta(1.5 nm) Pd(3 nm) [Co(0.28 nm)Pd(0.9 nm)] x8 Pd(1.1 nm), deposited at room temperature in 3 mTorr Ar pressure via magneton sputtering. In contrast to previous samples used for BPM fabrication, we did not use blanket deposition of the media onto prepatterned substrates, but subsequent patterning of an initially continuous multilayer film, in order to avoid the presence of magnetic trench material. Thus for patterning the samples were coated with 1-nm Ta, 1-nm Si, and 20-nm DLC. Dot arrays with periods from 1 μm to 45 nm were patterned in 200 μm $\times$ 200 μm areas by e-beam lithography in ZEP 520A resist. The samples were developed in n-amyl acetate at 2 °C under ultrasonic agitation for 30 sec. The e-beam pattern was reversed by a lift-off of 10 nm of Cr. The pattern was then etched into the DLC with a CO_2 reactive ion etch and the patterns were milled with a 200 V Ar beam at a 5° angle with the normal to the sample surface.

[20]J. Hohlfeld, S. S. Wellershoff, J. Gudde, U. Conrad, V. Jahnke, and E. Matthias, Chem. Phys. **251**, 237 (2000).

[21]S. Datta and B. J. Hunsinger, J. Appl. Phys. **50**, 5661 (1979).

[22]D. Nardi, F. Banfi, C. Giannetti, B. Revaz, G. Ferrini, and F. Parmigiani, Phys. Rev. B **80**, 104119 (2009).

[23]D. Nardi, M. Travagliati, M. E. Siemens, Q. Li, M. M. Murnane, H. C. Kapteyn, G. Ferrini, F. Parmigiani, and F. Banfi, Nano Lett. **11**, 4126 (2011).

[24]K. A. Nelson, R. J. D. Miller, D. R. Lutz, and M. D. Fayer, J. Appl. Phys. **53**, 1144 (1982).

[25]S. Kinoshita, Y. Shimada, W. Tsurumaki, M. Yamaguchi, and T. Yagi, Rev. Sci. Instrum. **64**, 3384 (1993).

[26]C. Klieber, E. Peronne, K. Katayama, J. Choi, M. Yamaguchi, T. Pezeril, and K. A. Nelson, Appl. Phys. Lett. **98**, 211908 (2011).

[27]D. H. Hurley, R. Lewis, O. B. Wright, and O. Matsuda, Appl. Phys. Lett. **93**, 113101 (2008).